

Tuning the Magnetic Properties of Hard–Soft $\text{SrFe}_{12}\text{O}_{19}/\text{CoFe}_2\text{O}_4$ Nanostructures via Composition/Interphase Coupling

Published as part of The Journal of Physical Chemistry virtual special issue “D. D. Sarma Festschrift”.

Pierfrancesco Maltoni,* Tapati Sarkar, Gianni Barucca, Gaspare Varvaro, Federico Locardi, Davide Peddis,* and Roland Mathieu*

Cite This: *J. Phys. Chem. C* 2021, 125, 5927–5936

Read Online

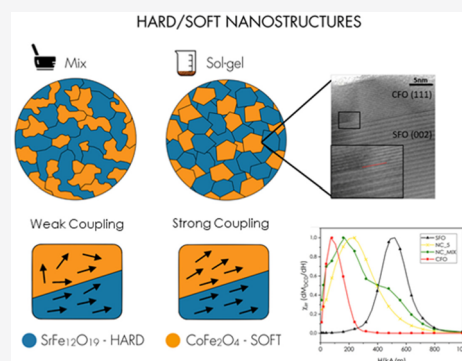
ACCESS |

Metrics & More

Article Recommendations

Supporting Information

ABSTRACT: Magnetic nanocomposites (NCs) are extremely appealing for a wide range of energy-related technological applications, specifically as building blocks for next-generation permanent magnets. The design of such nanostructures requires precise chemical synthesis methods, which will permit the fine-tuning of the magnetic properties. Here we present an in-depth structural, morphological and magnetic characterization of ferrite-based nanostructures obtained through a bottom-up sol–gel approach. The combination of the high coercivity of a hard phase $\text{SrFe}_{12}\text{O}_{19}$ (SFO) and the high saturation magnetization of a soft phase, CoFe_2O_4 (CFO), allowed us to develop exchange-coupled bimagnetic NCs. A symbiotic effect is observed in a SFO/CFO nanocomposite, as the unique oriented growth of SFO prevents grain growth of the CFO, thus restricting the crystallite size of both. Through X-ray powder diffraction (XRPD), transmission electron microscopy (TEM), and magnetic measurements we clarify the relationship between the distribution and size of hard/soft particles, the optimization of interfaces and the obtained uniform magnetic response. This study allowed us to establish the potentiality of hard/soft SFO/CFO nanostructures in current permanent magnet technology.



1. INTRODUCTION

Magnetic nanostructures have gained a lot of interest over the past years because of the possibility to finely tune their properties on the nanoscale.^{1–3} Technological and scientific interests include a wide range of applications, such as spintronic/multiferroic systems,^{4,5} electromagnetic functions such as electromagnetic wave absorption and shielding,⁶ energy devices,⁷ and water electrolysis.⁸ Nanosystems have also been proposed as building blocks for next-generation permanent magnets (PMs).^{2,9} Such magnets are used nearly everywhere including in energy-related applications, ranging from wind power, magnetocaloric refrigeration, and recently electric vehicles.¹⁰ Indeed, their use is so widespread that there is an ever-growing demand for PMs. Currently, the vast majority of PMs contains rare earth elements (REEs), which are disadvantageous due to critical issues regarding their supply and environmental impact.¹⁰ This scenario has stimulated an intense activity for the quest of new nanomaterials, as well as the enhancement of the properties of materials currently used, with a reduced or even zero content of REEs.¹¹ In this regard, ferrites have shown to be a promising class of materials, in particular M-type $\text{SrFe}_{12}\text{O}_{19}$ magnets, which show the best magnetic performance among ferrites (energy products of 40–460 kJ m^{−3}).^{12,13} Many synthesis procedures have been

investigated as a potential strategy to develop nanostructured ferrites through different bottom-up approaches.^{12,14–17} In this regard, among the diversified ways investigated so far, exchange coupled hard/soft nanocomposites (NCs) have received significant attention.^{18,19} Our recent studies on magnetic NCs clearly show that the synthesis strategy plays a critical role in the extent of magnetic coupling that can be achieved between the phases.^{20–22} This strongly depends on many parameters, such as the degree of particle agglomeration of each individual phase and specifically the nature of the interface, which must be optimized to obtain a maximum interfacial contact. To achieve high performances, PMs ideally require a squared magnetization loop to keep as much of the magnetization as possible within the magnet: specifically, a strong saturation magnetization (M_s) together with a high remanent magnetization (M_R) combined with a high coercivity (H_C) (i.e., high resistance to demagnetization).^{13,23} Despite

Received: January 14, 2021

Revised: February 19, 2021

Published: March 5, 2021



Table 1. List of Samples, Nominal Composition, and Weight Ratio (mg/mg) for Sr/Fe and Co/Fe in the Respective SFO and CFO Phases Obtained by ICP Analysis

ID	composition (w/w %)	ICP		synthesis method
		Sr/Fe	Co/Fe	
SFO	SrFe ₁₂ O ₁₉	0.13		self-combustion sol–gel
CFO	CoFe ₂ O ₄		0.48	
NC_1	SrFe ₁₂ O ₁₉ /CoFe ₂ O ₄ 90/10	0.13	0.48	one-pot self-combustion sol–gel
NC_2	SrFe ₁₂ O ₁₉ /CoFe ₂ O ₄ 80/20	0.13	0.51	
NC_3	SrFe ₁₂ O ₁₉ /CoFe ₂ O ₄ 70/30	0.13	0.49	
NC_4	SrFe ₁₂ O ₁₉ /CoFe ₂ O ₄ 60/40	0.14	0.48	
NC_5	SrFe ₁₂ O ₁₉ /CoFe ₂ O ₄ 50/50	0.13	0.48	
NC_MIX	SrFe ₁₂ O ₁₉ /CoFe ₂ O ₄ 50/50			physical mixing

considerable efforts, usually all these values cannot be maximized simultaneously in the same material. Hence, coupling materials with intrinsically different physical properties could result in nanocomposites prototypical of a new category of magnets.^{2,24} For these reasons, several studies on ferrite-based NCs can be found in the literature, covering composites prepared as powders by physical mixing of the two phases, or by different chemical one-pot synthesis,^{20,24–26} as multilayers films^{27,28} and as dense ceramic pellets by spark plasma sintering,²⁹ or warm compaction.¹⁷ Nevertheless, the lack of comprehensive studies on the degree of magnetic coupling in such systems is rather broad. In this regard, we have recently investigated the role of synthesis strategy in controlling the magnetic coupling of bimagnetic systems.^{21,22} In this paper we report an extensive investigation on various SrFe₁₂O₁₉/CoFe₂O₄ (SFO/CFO) NCs covering a range of compositions, which were synthesized through a one-step combustion sol–gel approach, adapted from our previous strategies.¹⁶ They consist of a hard-magnetic phase SFO, with a high magnetocrystalline anisotropy constant ($K = 0.35 \text{ MJ/m}^3$) and high magnetic uniaxial anisotropy along the c -axis,^{30,31} and a soft phase CFO, with a higher M_s (0.45 MA/m).²³ The phenomenon known as exchange coupling rises from the exchange interactions among the two ferrimagnetic phases at the nanoscale;^{1,24} the hard phase supplies the necessary magnetic anisotropy and prevents the coupled soft phase from demagnetizing. Hereby the evolution of the magnetic properties was studied as a function of the particle size and shape, particularly focusing on the magnetic coupling at the interface that can be obtained thanks to the unique synthesis method. To the best of our knowledge, this is the first comprehensive study clarifying the relationship between morphology, structure, and magnetic coupling of SFO/CFO NCs obtained through a self-combustion sol–gel approach. In this work, we will show that it is fundamental to carefully control the size and distribution of the soft/hard-phase regions to limit the deterioration of the desired magnetic performance and achieve efficiently coupled NCs.

2. EXPERIMENTAL DETAILS

2.1. Synthesis. In this section, we describe the synthesis strategies adopted to prepare a family of ferrite-based nanostructures (see the [Supporting Information](#)).

NCs. To prepare five exchange-coupled hard/soft SFO/CFO nanocomposites (NCs), with compositions ranging from 50/50 to 90/10 w/w % (in steps of 10%), a one-pot sol–gel route was used¹⁶ (more details in the [Supporting Informa-](#)

[tion](#)): two separate sols were first prepared by dissolving stoichiometric amounts of the precursors of SFO, i.e., Fe(NO₃)₃·9H₂O and Sr(NO₃)₂·6H₂O (Sigma-Aldrich) in a [Fe³⁺]:[Sr²⁺] ratio of 11:1, and the precursors of CFO, i.e., Co(NO₃)₂·6H₂O and Fe(NO₃)₃·9H₂O (Sigma-Aldrich) in a [Fe³⁺]:[Co²⁺] ratio of 2:1, respectively, in deionized water (DI) in a beaker at room temperature to give a Fe³⁺ concentration of 0.1 M. Then a 1 M citric acid aqueous dispersion was added (molar ratio of total metals to citric acid 1:1) to these solutions and mixed for 30 min at 40 °C to improve the solubility of the nitrates and thus the chelating efficiency of the ligand. Subsequently, the dispersions were mixed for a further 10 min. After the mixture was cooled to room temperature, the pH was adjusted to 7 by adding NH₃ (30%, Sigma-Aldrich) dropwise. Next, it was heated on a hot plate to 80 °C to form a gel, thanks to the chelating action of the citric acid. After the entire solution was converted to a dry gel (after ~6 h), the temperature was rapidly increased to 300 °C, inducing a flameless self-combustion. The obtained dry powders were ground and annealed at 950 °C for 3 h with a ramp of 5 °C/min under air, thus resulting in biphasic NCs. We refer to these in the rest of the article as NC_1, NC_2, NC_3, NC_4, and NC_5.

SFO and CFO. For comparison, the parent materials (SrFe₁₂O₁₉ and CoFe₂O₄) were prepared by the self-combustion sol–gel approach using the single sols; then the obtained dry powders were ground and annealed (following a similar procedure of NCs). We refer to these samples as SFO and CFO, respectively.

NC_MIX. To prepare NC_MIX, the two individual components prepared in their as-burn forms after the combustion were physically mixed in a mortar with acetone to obtain a fine mixture of the two powders, with a weight fraction SFO/CFO = 50/50%. For comparison, the product was annealed at 950 °C for 3 h in air, as the NCs.

All the samples were washed with 1 M HNO₃ and several times with DI water and finally dried in an oven at 80 °C ([Figure S3](#) depicts that the treatment does not affect the structure in any way). The samples are summarized in [Table 1](#).

The evolution of the reaction from the gel, through as burnt and to annealed powders, was checked by means of Fourier-transform infrared spectroscopy (FT-IR): the spectra were acquired with a Shimadzu IRPrestige-21, equipped with a Specac Golden Gate single reflection diamond attenuated total reflection (ATR). All samples were analyzed in the region between 4000 and 450 cm^{−1}.

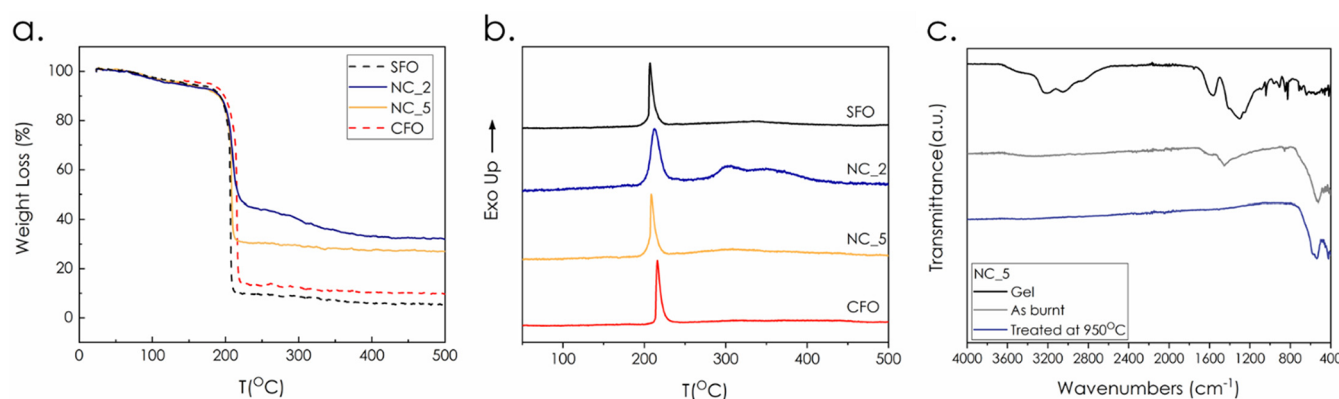


Figure 1. (a) TG and (b) DTA curves of SFO, CFO, and NC_2 and NC_5 gels before self-combustion. (c) Evolution of FTIR spectra of NC_5 from gel to thermally treated.

2.2. Characterization and Data Treatment. The powder samples were characterized by using a Bruker D8 Advance diffractometer (solid state rapid LynxEye detector, Cu K α radiation, Bragg–Brentano geometry, DIFFRACT plus software) in the 10°–140° 2 θ range with a step size of 0.013° (counting time was 4 s per step). The powder samples were grounded in an agate mortar and suspended in ethanol. A Si substrate was covered with several drops of the resulting suspension, leaving randomly oriented crystallites after drying. Rietveld analysis was performed on the X-ray powder diffraction (XRPD) data by using the FULLPROF program.³² The diffraction peaks were described by a modified Thompson–Cox–Hastings pseudo-Voigt function. A peak asymmetry correction was made for angles below 40° (2 θ). Background intensities were estimated by interpolating between up to 60 selected points. In the Rietveld model, the CoFe₂O₄ was described assuming a Co:Fe stoichiometry of 1:2 and a random cationic distribution between the crystallographic sites (equivalent). A NIST LaB₆ 660b standard was measured under the same conditions as the samples to account for the instrumental contribution to the peak broadening.

Transmission electron microscopy (TEM) analysis was performed by using a Philips CM200 microscope operating at 200 kV and equipped with a LaB₆ filament. For TEM observations, the samples, in the form of powder, were prepared by using the following procedure. A small quantity of powder was dispersed in ethanol and subjected to ultrasonic agitation for ~1 min. A drop of the suspension was deposited on a commercial TEM grid covered with a thin carbon film. Finally, the grid was kept in air until complete ethanol evaporation.

Magnetic measurements were performed at room temperature ($T = 300$ K) by using a Quantum Design superconducting quantum interference device (SQUID) magnetometer, which can supply a maximum field of 5 T. To avoid any displacement of the nanopowders during the measurements, the samples were immobilized in a glue (no significant magnetic contribution from the glue was observed). Isothermal field-dependent magnetization loops were recorded by sweeping the field in the -5 T to $+5$ T range, and the obtained magnetization values were normalized by the weight of powders present in the sample and expressed in Am²/kg. To get information about the irreversible processes, direct current demagnetization (DCD) remanence curves were measured by applying a progressively higher DC reverse field to a sample

previously saturated under a field of -5 T and by recording, for each step, the value of the remanent magnetization, which was then plotted as a function of the reverse field. All the measurements were corrected by considering the demagnetizing factor (DMF) for packed particles (NP) in a dense system $\varphi \sim 0.3$ and a spherical shape for the particles (more details are reported in the Supporting Information).³³ The maximum energy product $(BH)_{\text{MAX}}$ was estimated to quantify the maximum amount of magnetic energy storable in a permanent magnet²³ (more details in Figure S11). To evaluate it, the theoretical densities of SFO (5100 kg/m³) and CFO (5290 kg/m³) were used, as reported by the following equation: $\rho_{\text{NC}} = x\rho_{\text{SFO}} + (1 - x)\rho_{\text{CFO}}$, where ρ_{NC} is the density of the NC, ρ_{SFO} is the density of SFO, ρ_{CFO} is the density of CFO, and x is the volume fraction of SFO in the NC.

Inductively coupled plasma optical emission spectroscopy (ICP-OES) was performed for elemental analysis with an iCAP 6300 DUP ICP-OES spectrometer (ThermoScientific). The samples were digested in aqua regia (HCl 37% v/v–HNO₃ 69% v/v 3:1) for 8 h, then diluted by using Milli-Q water, and analyzed. Differential thermal analysis (DTA)/thermogravimetric analysis (TGA) were performed by using a LabsysEvo 1600 DTA/TGA (Setaram). One milligram of gel and 10 mg of sample obtained after self-combustion were put in an alumina crucible and heated from 30 to 1000 °C at 10 °C/min under an O₂ atmosphere (20 mL/min). The DTA and TGA curves were elaborated by using the dedicated software Calisto (Setaram).

3. RESULTS AND DISCUSSION

3.1. Synthesis Process. To elucidate the synthesis method, thermal analysis and infrared spectroscopy have been performed on the precursor gels before self-combustion. The corresponding TG and DTA curves are shown in Figures 1a,b. The TG curves reveal that the self-combustion process for the gels of SFO and CFO occurs between 190 and 240 °C, as indicated by a sharp weight loss around 210 °C (Figure 1a), combined with a strong exothermic peak. On the other hand, the NCs display a further variation linked to the different composition. Indeed, at higher temperature, the TG curve for NC_2 (blue curves) displays a consecutive weight loss in a wide range of temperature (between 200 and 300 °C). The corresponding DTA curve showed two exothermic peaks centered at 300 and 350 °C, respectively (Figure 1b). However, by increasing the amount of CFO, the NC_5

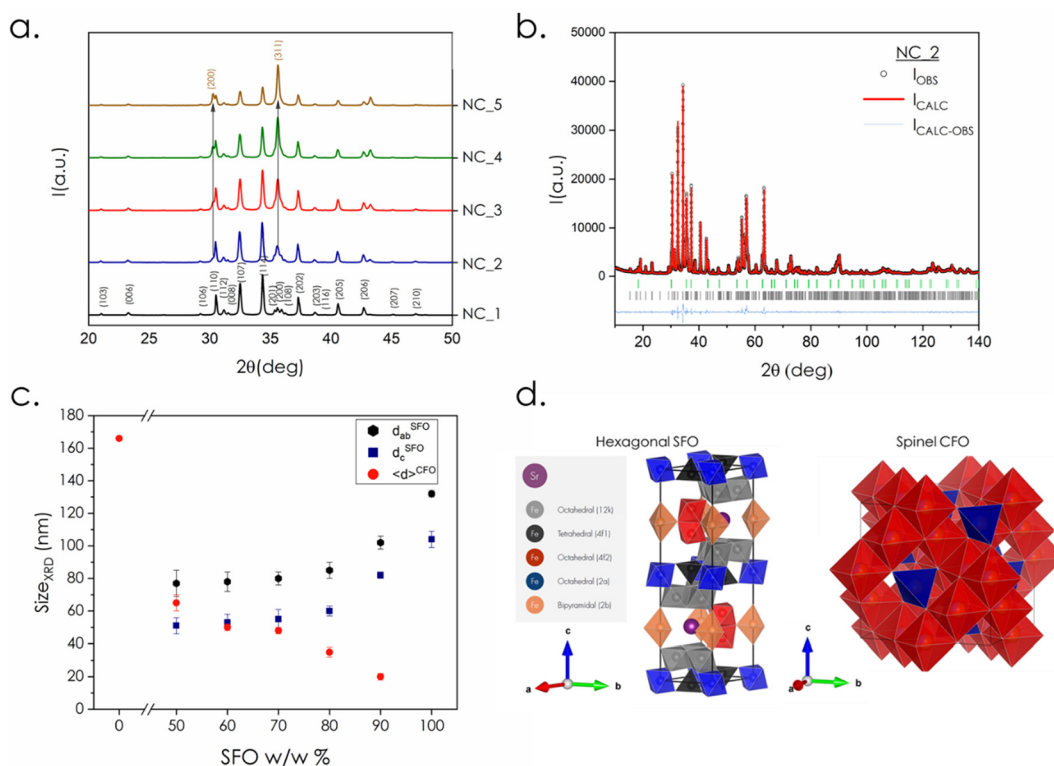


Figure 2. (a) XRPD patterns of the NCs. (b) Rietveld refinement results for NC_2. (c) Particle size as a function of NCs phase composition and (d) unit cells for SFO and CFO obtained by using VESTA⁴¹ according to the refined SFO and random model for spinel structure (tetrahedral and octahedral sites are indicated with blue and red polyhedrons, respectively).

(yellow curve) behaves similarly to SFO and CFO, showing a single combustion process. Additionally, the TG curves obtained on the samples after self-combustion (Figure S4) indicate that the complete formation of the desired crystalline phases is obtained only at higher temperature than the first combustion of the gel at 200 °C. Then, interestingly the weight loss is significantly reduced moving to NC_5 (yellow curve), that is, ~3%. We could also observe a further small loss at higher T (~600–700 °C) for all the samples, except for CFO, that might be ascribed to the rearrangement of Fe and Sr oxides in giving the final SFO phase.³⁴ These are a first evidence that the reaction proceeds at lower temperature (below 300 °C) in a symbiotic way: by increasing CFO from NC_2 to NC_5, the formation of SFO precursors is assisted, thus obtaining first CFO and the precursors of SFO maintaining a low synthesis temperature. The exact composition of the amorphous phases can be probed by using detailed elemental analysis, but this is out of the scope of the present paper.

As an example, FTIR spectra are also reported for the NC_5 as gel, after combustion powder, and finally the thermally treated sample in Figure 1c: these confirm the preliminary results obtained by thermal analysis. Even if a fine analysis is nontrivial on this system, we were able to follow the evolution of the reaction. For the gel, the signals in the regions 1000–1600 and 2800–3400 cm^{-1} can be attributed to the presence of the citric acid-based network of the xerogel,³⁵ and the one at 3400–3600 cm^{-1} is attributed to some residual water in the dried gel. After the combustion, the signals in the region 400–600 cm^{-1} , ascribed to the stretching modes of the metal-oxygen bond,^{36–38} become stronger, whereas small residuals of gel are still present. Eventually, after the thermal treatment at

950 °C, the signals due to the main phases are only present. Furthermore, the spectra for NCs after combustion (Figure S5a) support the thermal analysis as the intensity of the SFO phase-related peaks increases considerably with respect to single CFO.

3.2. Structural and Morphological Characterization.

The XRPD patterns of the NCs (Figure 2a) show that most of the reflections can be ascribed to the hexagonal structure typical of strontium hexaferrite, with space group $P6_3/mmc$.³⁹ The reflections due to the CFO phase are not visible in NC_1 because of the low intensity and the overlapping with more intense SFO ones; the characteristic (311) reflection appears when the amount of CFO is increased and becomes clearly visible in NC_5. This reflection can be ascribed to a spinel structure ($Fd\bar{3}m$),¹⁹ as clearly evidenced by analyzing the XRD spectrum of NC_5 just after the combustion (Figure S6). At this stage of the synthesis, the appearance of a well-crystallized phase is observed and identified as the spinel CFO phase. In agreement with our previous studies,¹⁶ a higher temperature is required for the complete formation of the hexagonal SFO phase as also confirmed by thermal analysis. A temperature of 950 °C was chosen for the calcination of the as-burnt NCs to guarantee a homogeneous growth of both the phases based on the synthesis conditions (Fe:Sr ratio of 11:1).

Rietveld analysis was performed by modeling the SFO as a hexagonal phase ($P6_3/mmc$, number 194)³⁹ and the CFO as a spinel ($Fd\bar{3}m$, number 227).¹⁹ The stoichiometry of both compounds was checked by ICP, confirming the expected composition. As an example, the XRPD pattern analyzed by Rietveld refinement is shown in Figure 2b, highlighting the distinct phases. The extracted lattice parameters are shown in Table 2. Interestingly, regarding the SFO phase, we can

Table 2. Lattice Parameters (a , b , and c), Apparent Sizes (d_{ab} and d_c for SFO, $\langle d \rangle^{\text{CFO}}$ for CFO) Extracted from Rietveld Refinement and Plate Ratio for SFO (R) (Uncertainties in the Last Digit Are Given in Parentheses)

ID	SFO		CFO		d_{ab} (nm)	d_c (nm)	$\langle d \rangle^{\text{CFO}}$ (nm)	R
	$a = b$ (Å)	c (Å)	$a = b = c$ (Å)					
SFO	5.88083(1)	23.05491(4)			132(2)	104(5)		1.26
NC_1	5.88124(1)	23.05310(9)	8.38149 (7)		103(4)	82(2)	20(2)	1.26
NC_2	5.88069(1)	23.04252(9)	8.38354(7)		85 (5)	60(3)	35(2)	1.42
NC_3	5.88068(2)	23.03823(8)	8.38296(4)		80(4)	55(6)	48(3)	1.45
NC_4	5.88055(2)	23.03539(8)	8.38301(1)		78(6)	53(5)	50 (2)	1.47
NC_5	5.87914 (2)	23.03527(4)	8.38283(3)		77(8)	51(5)	65(2)	1.50
CFO			8.38246 (2)				166(1)	

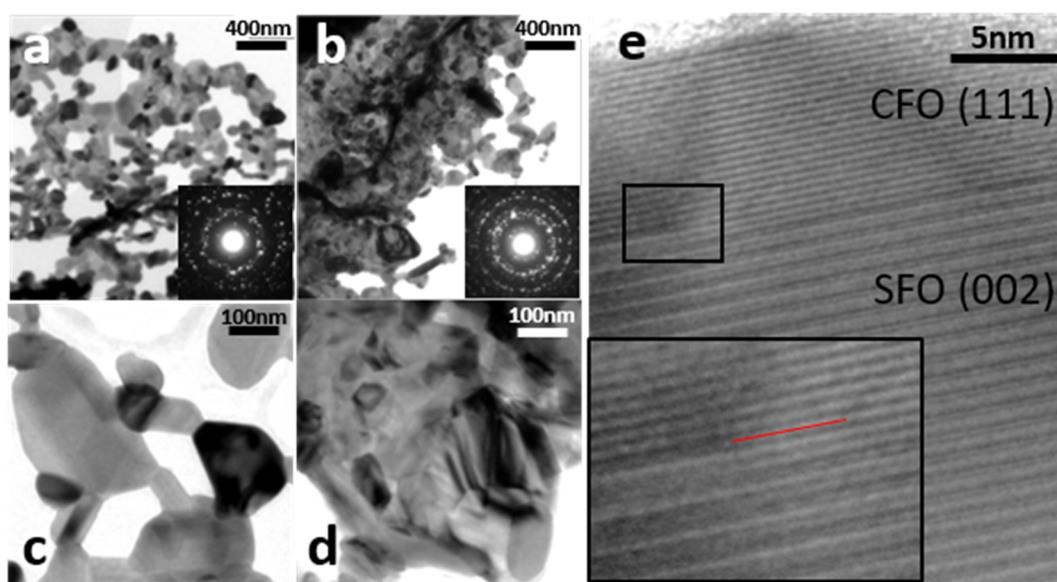


Figure 3. Bright-field TEM images showing the nanocomposites structure: (a, c) NC_1, (b, d) NC_4; SAED patterns are reported in the insets of the respective figures. (e) High-resolution (HR) TEM image showing the oriented growth of the SFO and CFO phases in NC_4; inset reveals the presence of a dislocation (red line) at the phases interface.

observe a slight constant reduction of $a = b$ and c lattice parameters, from NC_1 to NC_5, hinting at a possible confinement effect due to the presence of a higher amount of CFO. Any impurities of $\alpha\text{-Fe}_2\text{O}_3$ or SrCO_3 as secondary phases were not detected.

Based on our previous study,¹⁶ the SFO crystallite sizes have been obtained by considering a platelet shape with the normal along the crystallographic c -axis (001) and adopting the vector size model in FULLPROF. We define the size extracted along the ab -plane and along the c -axis as d_{ab} and d_c , respectively. In addition to this, a March–Dollase model has been used taking into consideration a preferred orientation along the (001) Bragg direction to evaluate the platelet-like orientation of the ferrites.⁴⁰ The analysis of peak broadening in the patterns unambiguously evidences a size dependence of SFO on the amount of CFO. The d_{ab} and d_c sizes decrease from 132(2) to 77(8) nm and from 104(5) to 51(5) nm, respectively, from single-phase SFO to NC_5 (Figure 2c and Table 2). The CFO amount affects considerably the size of SFO and CFO because of the restriction on the growth of one phase by the other. We define the parameter R as the aspect ratio ($R = d_{ab}/d_c$) of the platelets (Table 2), revealing a more plate-like morphology when the weight percentage of CFO is raised. Besides, we

notice an evident step between NC_1 and NC_2 as R changes from 1.26 to 1.42 and remains almost constant until NC_5, suggesting a threshold value in the fraction of CFO. This shows that the one-pot sol–gel synthesis technique allows us to control the size/shape of the nanocrystallites as well as the aspect ratio of the grains. All the refined XRPD patterns are presented in Figure S7, together with the corresponding parameters and refinement quality factors (Tables S1–S3). In addition, Figure 2d shows the representations of the single unit cells for SFO and CFO by using VESTA.⁴¹

The inner structure of the NCs was further investigated by transmission electron microscopy (TEM) techniques revealing that all the samples are composed of interconnected particles forming porous aggregates. Increasing the CFO concentration, the porosity of the aggregates seems to reduce, as can be deduced by comparing Figures 3a and 3b relating to NC_1 and NC_4, respectively. In NC_1, the particles are like pieces of a mosaic linked together on one or more sides that give rise to a porous structure. On the other hand, the NC_4 particles appear more aggregated and pores are not easily detectable.

The different particles density is confirmed by the selected area electron diffraction (SAED) patterns shown in the insets of the images. They were taken under the same microscopy

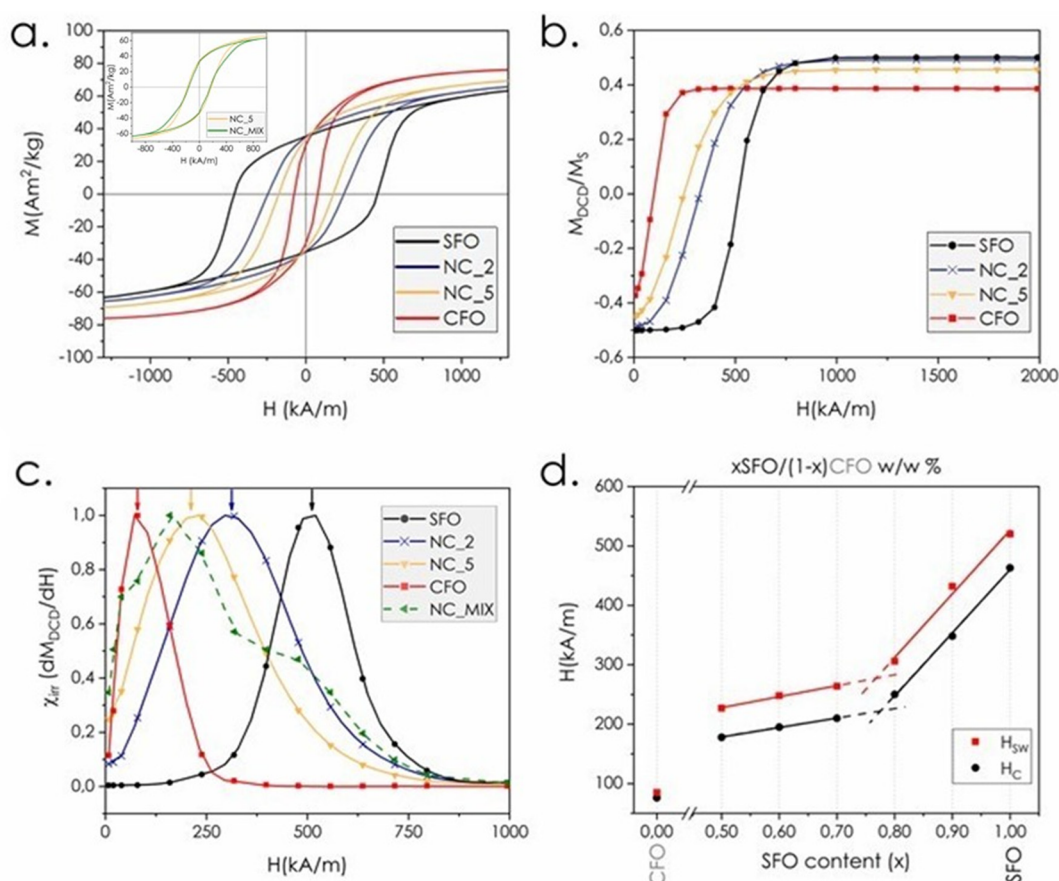


Figure 4. (a) Magnetization M vs magnetic field H curves for SFO, NC₂, NC₅, and CFO; comparison between M vs H curves for NC₅ and NC_{MIX} is reported in the inset. (b) Magnetization M_{DCD}/M_s vs magnetic field H curves for SFO, NC₂, NC₅, and CFO, and (c) corresponding normalized switching field distributions (SFD) at 300 K; SFD for NC_{MIX} is also shown. (d) (H_C) coercive field and average switching field (H_{SW}) determined from the magnetization measurements as a function of SFO fraction in the NCs.

conditions and clearly reveal a larger number of diffraction spots for NC₄ (inset of Figure 3b) with respect to NC₁ (inset of Figure 3a). All the diffraction spots can be associated with the SFO and CFO phases (i.e., no other phases have been detected), confirming the XRPD results. High-resolution (HR) TEM analysis has allowed to investigate the structure of the samples further. Notably, the same kind of oriented growth between the SFO and CFO phases was observed in all the NCs. In more detail, Figure 3e shows the CFO (111) atomic planes that become SFO (002), scrolling toward the bottom of the image. A careful look at the interface between the two phases (inset of Figure 3e) reveals how the transition is accompanied by the formation of dislocations (the red line shows an interrupted (111) CFO plane), suggesting a strong interaction between the two crystallographic structures. The particles have a typical plate-like shape for low concentration of CFO, as can be seen in Figure 3c relating to NC₁. However, as the CFO concentration increases, the plate-like shape seems to be lost, Figure 3d relating to NC₄. For the sake of clarity, it is important to stress that the nanocrystallites, investigated by XRD, form the particles observed by TEM (a particle can be composed of one or more crystallites), so the shape of the particles may hence be different from the nanocrystallites' one. The growth of a phase over the other can explain both the tendency of the particles to lose the plate-like shape, typical of the SFO phase, as the CFO concentration increases, and the size/shape behavior of the nanocrystallites determined by X-

ray diffraction. Indeed, it is reasonable to assume that if the CFO grains act as nucleation sites for the SFO phase, a greater number of nucleation sites will reduce the final average sizes of the SFO grains (the total mass of the SFO phase is distributed over a greater number of grains, increasing the CFO concentration); moreover, the presence of the SFO phase inhibits the growth of some CFO grains at the expense of others CFO ones (typically smaller). At the end we obtain nanocrystallites (not particles) having a smaller size with respect to the pure CFO and SFO phases and the SFO crystallites having a more marked plate-like shape.

3.3. Magnetic Coupling in Biphasic Nanocomposites.

To clarify the relationship between the morphostructural features and interface magnetic coupling, field-dependent magnetization loops recorded at 300 K for NC₂, NC₅, SFO, and CFO are reported in Figure 4a. All the curves exhibit a single reversal process of magnetization, suggesting that the two magnetic phases are homogeneously dispersed and strongly magnetically coupled^{21,24} because of the efficiency of the one-pot sol-gel method.^{16,22} The corresponding magnetization loops of all the NCs are included in Figure S8. The NCs show an intermediate magnetic behavior between the two individual phases, as proved by the comparison of the parameters reported in Table 3. The M_s values increase with respect to the corresponding values of SFO due to the CFO phase, whereas the M_R/M_s increases for NC₁ and NC₂ and remains similar to SFO for the other NCs. In addition, the

Table 3. Saturation Magnetization (M_s) Estimated as $M(H = 4 \text{ MA/m})$, Reduced Remanence Magnetization M_R/M_s , Coercive Field (H_C), Average Switching Field (H_{SW}) Measured at 300 K, and Energy Product $(BH)_{MAX}$

ID	M_s (Am ² /kg)	M_R/M_s	H_C (kA/m)	H_{SW} (kA/m)	$(BH)_{MAX}$ (kJ/m ³)
SFO	69.9 (5)	0.50	463(5)	520(5)	9.5
NC_1	70.4(8)	0.49	348(4)	432(4)	9.1
NC_2	71.8(4)	0.49	250(3)	306(2)	9.2
NC_3	72.5(7)	0.47	210(2)	264(2)	8.9
NC_4	73.2(4)	0.47	195(2)	248(3)	8.7
NC_5	74.0(5)	0.45	178(2)	227(2)	8.4
CFO	78.3(6)	0.38	76(7)	85 (4)	6.0

variation of H_C is consistent with the increasing amount of soft phase (up to 50 w/w %). These results suggest a good degree of magnetic coupling between the phases.

To investigate the magnetic behavior of the NCs in more detail, we have performed direct current demagnetization (DCD) measurements⁴² allowing to study the irreversible process of magnetization.²⁰ The M_{DCD} (normalized over the M_s of each sample) versus reverse magnetic field (H) for the corresponding NCs as well as the first-order differentiated curves of M_{DCD} with respect to H (switching field distributions (SFDs)), normalized to ease the comparison, are displayed in Figures 4b and 4c, respectively; the latter represents the irreversible component of the susceptibility (χ_{irr}). This quantity can be viewed as a measure of the energy barrier distribution (which is associated with the distribution of particle's switching field when we consider nanoparticle-based systems), defined as the field necessary to overcome the energy barrier during an irreversible reversal process.^{43–45} NC_2 and NC_5 clearly show a single reversal process of magnetization with CFO and SFO phases strongly coupled, with an intermediate H_{SW} value compared to that of the CFO and SFO single phases, thus proving the efficiency of controlling the size and distribution of hard/soft-phase regions thanks to the synthesis method (see Figure S8 for data for all NCs).

To demonstrate the efficiency of our method, we have also prepared a NC_{MIX} sample by physically mixing the starting precursor SFO and CFO phases: at a first glance, the M vs H

loop seems similar to those of the NCs (see the inset in Figure 4a, Figure S9 for a larger view). The apparent qualitative (i.e., shape of the hysteresis loop) and quantitative (values of M_s and H_C) similarities might erroneously suggest that the sample shows almost the same physical properties independently of the different synthesis method. However, the $M_{DCD}(H)$ data and associated SFD (see Figure 4c) reveal two contributions, centered at magnetic fields that can be attributed to the reversal processes of the two individual phases (SFO and CFO), and that of a system with an additional contribution between them, close to the NC_5 one, i.e., an imperfectly coupled system.⁴⁶

A further evaluation of the coercive field of the NCs is necessary to assess their potential as building blocks in permanent magnets application. Although saturation magnetization increases monotonously with the fraction of CFO, the coercive field exhibits a nonmonotonic behavior. As depicted in Figure 4d, we notice two different linear trends in H_C (as well as in H_{SW}), strongly dependent on the weight percentage of soft phase introduced in the composite: starting from single-phased SFO, the coercive field consistently drops by adding 10% CFO, as the interactions within the hard matrix are weakened. This event is more dramatic when we move to 20% and then 30%, when the values slightly decrease, to become then almost constant: this may be related to the CFO fraction threshold value discussed above, beyond which the soft phase affects the aspect ratio and the overall magnetic properties, indicated by the intersection between the linear fittings (~ 25 CFO w/w %). Thus, the soft phase triggers a possible deterioration mechanism of the hard matrix, depending on its volume fraction.⁴⁷ According to the limit of perfect exchange coupling,¹ $H_C = H_H(1 - f)$ (where H_H refers to the coercivity of the hard phase, 463 kA/m in our case, and f to the volume fraction of the soft one), the coercivity should follow a linear trend. Our experimental results seem to be in good agreement, although other factors need to be considered, such as real-structure imperfections, distribution of the soft phase in the hard matrix, and the quality of their interface, which lead to a disparity between the theoretical and real behavior.¹ In this regard, we must point out that NC_1 and NC_5 show a magnetic performance closer to the limit of exchange coupling, evidently because our synthesis method guarantees a higher degree of homogeneity in the obtained distribution and

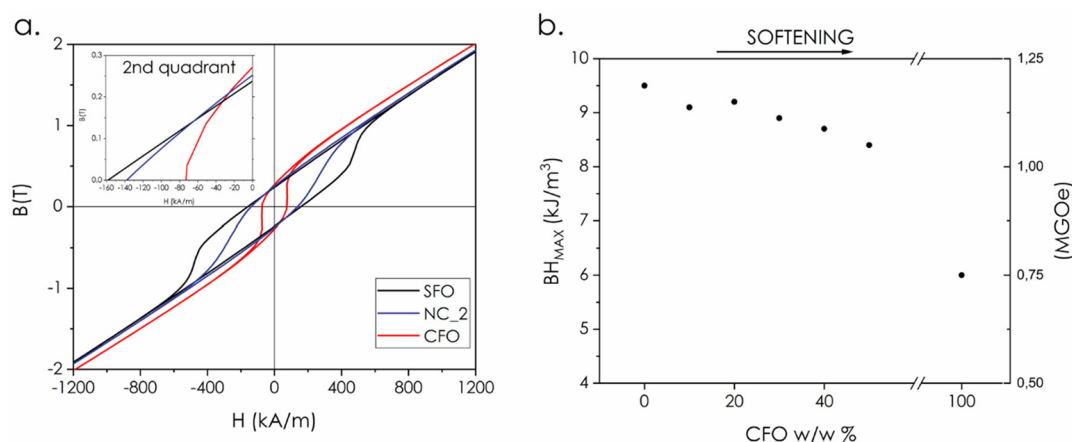


Figure 5. (a) Magnetic flux B (T) vs field H (kA/m) loops for SFO, CFO, and NC_2. (b) $(BH)_{MAX}$ at 300 K (in kJ/m³ and for reference in MGOe) as a function of the fraction of CFO.

therefore a better magnetic performance compared to other approaches.^{48,49} Upon comparison of their performance in terms of $(BH)_{\text{MAX}}$ (Table 3), the energy products consistently decrease by increasing the soft phase with respect to hard SFO, revealing that CFO does not improve the performance of the main phase because the remanence does not undergo a positive variation (Figure 5a), although M_s is enhanced. However, it is clear from our study that by carefully controlling the size and distribution of the soft-phase regions, it is possible to tune and limit the decrease of the coercivity to our desire to design nanocomposites with improved magnetic properties.

In this regard, it is noteworthy that the $(BH)_{\text{MAX}}$ product is bounded to $(BH)_{\text{MAX}} \leq (\mu_0 M_s)^2/4$ when $H_C > M_s/2$ for an archetypal rectangular hysteresis loop.^{50,51} In our case, H_C for SFO (463 kA/m), having a very high magnetocrystalline anisotropy, overcomes $M_s/2$ (176 kA/m), thus suggesting that only large M_s and M_R can efficiently increase the $(BH)_{\text{MAX}}$ product. This reveals to be true for all the NCs; however, the inclusion of an increasing softer phase lowers H_C toward the $M_s/2$ limit for NC_5. This illustrates that a first effort should address the choice or design of a highly anisotropic material to be used as the hard phase. The choice and fine optimization of the soft phase may be accomplished as a second step. To this aim several strategies can be exploited, such as doping diamagnetic divalent ions into both the phases^{22,52,53} or by modifying the shape and surface anisotropy of the hard phase.

4. CONCLUSION

The design of bimagnetic nanostructures requires optimized interfaces, a homogeneous distribution of hard/soft particles, and control over the size to achieve a uniform magnetic response. We have demonstrated that optimizing the synthesis could guarantee a significant control over the size and shape of the crystallites of the individual phases as well as the coupling between hard/soft ferrites in the NCs. In this regard, our sol-gel approach revealed to be efficient, in the realization of hard-soft exchange-coupled nanostructures, compared to physical mixing: the NCs show apparent similarities in their M vs H curves. Nevertheless, detailed and careful DC demagnetization measurements reveal very important differences in the degree of magnetic coupling in such systems. As far as we know, this is the first observation of such a symbiotic phenomenon in the development of ferrite-based NCs of SFO and CFO, where one phase (CFO) helps in the crystallization of the other one (SFO) by reducing the energy of formation of the second phase along a preferred orientation, hence acting as nucleation sites. Moreover, both phases prevent grain growth of each other. Through thermal analysis, XRPD, TEM, and magnetic measurements, we showed a significant relation between the structure, morphology (i.e., size and shape), and resulting magnetic properties of the obtained NCs, which show a well-defined physical and chemical structure. In particular, the evaluation of magnetic properties pointed out that the degree of magnetic coupling stems from the optimization of the interface between the hard/soft magnetic phases. Our results illustrate the suitability of the one-pot sol-gel method for finely tuning the size and shape of the individual phases in NCs as well as increasing the magnetic coupling via the strong interfacial coupling between the two phases. We believe that these results will provide a strong foundation for the further development of hard-soft phase-coupled NCs for permanent magnet applications.

■ ASSOCIATED CONTENT

Supporting Information

The Supporting Information is available free of charge at <https://pubs.acs.org/doi/10.1021/acs.jpcc.1c00355>.

Sample preparation; thermal analysis, FTIR, XRPD patterns and corresponding Rietveld refinement for SFO, CFO, and NCs; evaluation of demagnetizing factor and $(BH)_{\text{MAX}}$ product (PDF)

■ AUTHOR INFORMATION

Corresponding Authors

Pierfrancesco Maltoni – Department of Materials Science and Engineering, Uppsala University, SE-751 03 Uppsala, Sweden; orcid.org/0000-0001-9834-3164;

Email: pierfrancesco.maltoni@angstrom.uu.se

Davide Peddis – Institute of Structure of Matter, Italian National Research Council (CNR), 00015 Rome, Italy; Dipartimento di Chimica e Chimica Industriale, Università di Genova, I-16146 Genova, Italy; orcid.org/0000-0003-0810-8860; Email: davide.peddis@unige.it

Roland Mathieu – Department of Materials Science and Engineering, Uppsala University, SE-751 03 Uppsala, Sweden; orcid.org/0000-0002-5261-2047;

Email: roland.mathieu@angstrom.uu.se

Authors

Tapati Sarkar – Department of Materials Science and Engineering, Uppsala University, SE-751 03 Uppsala, Sweden; orcid.org/0000-0003-4754-2504

Gianni Barucca – Università Politecnica delle Marche SIMAU, 60131 Ancona, Italy

Gaspere Varvaro – Institute of Structure of Matter, Italian National Research Council (CNR), 00015 Rome, Italy; orcid.org/0000-0001-7313-7268

Federico Locardi – Dipartimento di Chimica e Chimica Industriale, Università di Genova, I-16146 Genova, Italy; orcid.org/0000-0002-1794-8282

Complete contact information is available at: <https://pubs.acs.org/doi/10.1021/acs.jpcc.1c00355>

Author Contributions

P.M., D.P., and R.M. conceived the experiments. P.M. synthesized the NCs. T.S. developed the synthesis method. XRD patterns were measured and analyzed by P.M. P.M. recorded and analyzed the magnetic data, which were critically discussed with R.M., T.S., G.V., and D.P. TEM and HRTEM measurements and data analysis were performed by G.B. Thermal analysis was by F.L., and the data were analyzed by P.M. FTIR was performed at CNR. P.M. wrote the manuscript, which was critically revised by all the authors. All authors have given approval to the final version of the manuscript.

Notes

The authors declare no competing financial interest.

■ ACKNOWLEDGMENTS

We thank the Swedish Energy Agency (project number 46561-1) and Swedish Research Council (VR) for financially supporting this work. T.S. acknowledges financial support from VR (starting grant no. 2017-05030). We are grateful to Dr. Francesco Soggia for the technical support provided during the preparation and the analysis of the samples by ICP-AES at the Università di Genova. P.M. thanks his colleague and friend

Dr. D. Joshi for the support during the magnetic measurements.

REFERENCES

- (1) Skomski, R.; Manchanda, P.; Kumar, P. K.; Balamurugan, B.; Kashyap, A.; Sellmyer, D. J. Predicting the Future of Permanent-Magnet Materials. *IEEE Trans. Magn.* **2013**, *49* (7), 3215–3220.
- (2) Balamurugan, B.; Sellmyer, D. J.; Hadjipanayis, G. C.; Skomski, R. Prospects for Nanoparticle-Based Permanent Magnets. *Scr. Mater.* **2012**, *67* (6), 542–547.
- (3) Sellmyer, D. J.; Balamurugan, B.; Das, B.; Mukherjee, P.; Skomski, R.; Hadjipanayis, G. C. Novel Structures and Physics of Nanomagnets (Invited). *J. Appl. Phys.* **2015**, *117* (17), 172609.
- (4) Ma, J.; Hu, J.; Li, Z.; Nan, C.-W. Recent Progress in Multiferroic Magnetoelectric Composites: From Bulk to Thin Films. *Adv. Mater.* **2011**, *23* (9), 1062–1087.
- (5) Anil Kumar, P.; Sarma, D. D. Effect of “Dipolar-Biasing” on the Tunability of Tunneling Magnetoresistance in Transition Metal Oxide Systems. *Appl. Phys. Lett.* **2012**, *100* (26), 262407.
- (6) Cao, M.; Wang, X.; Zhang, M.; Shu, J.; Cao, W.; Yang, H.; Fang, X.; Yuan, J. Electromagnetic Response and Energy Conversion for Functions and Devices in Low-Dimensional Materials. *Adv. Funct. Mater.* **2019**, *29* (25), 1807398.
- (7) Luo, Q.; Chen, H.; Lin, Y.; Du, H.; Hou, Q.; Hao, F.; Wang, N.; Guo, Z.; Huang, J. Discrete Iron(III) Oxide Nanoislands for Efficient and Photostable Perovskite Solar Cells. *Adv. Funct. Mater.* **2017**, *27* (34), 1702090.
- (8) Garcés-Pineda, F. A.; Blasco-Ahicart, M.; Nieto-Castro, D.; López, N.; Galán-Mascarós, J. R. Direct Magnetic Enhancement of Electrocatalytic Water Oxidation in Alkaline Media. *Nat. Energy* **2019**, *4* (6), 519–525.
- (9) Lewis, L. H.; Jiménez-Villacorta, F. Perspectives on Permanent Magnetic Materials for Energy Conversion and Power Generation. *Metall. Mater. Trans. A* **2013**, *44* (S1), 2–20.
- (10) Skokov, K. P.; Gutfleisch, O. Heavy Rare Earth Free, Free Rare Earth and Rare Earth Free Magnets - Vision and Reality. *Scr. Mater.* **2018**, *154*, 289–294.
- (11) Coey, J. M. D. Permanent Magnets: Plugging the Gap. *Scr. Mater.* **2012**, *67* (6), 524–529.
- (12) Saura-Múzquiz, M.; Granados-Mirallas, C.; Andersen, H. L.; Stingaciu, M.; Avdeev, M.; Christensen, M. Nanoengineered High-Performance Hexaferrite Magnets by Morphology-Induced Alignment of Tailored Nanoplatelets. *ACS Appl. Nano Mater.* **2018**, *1* (12), 6938–6949.
- (13) Eriksson, S.; Eklund, P. Effect of Magnetic Properties on Performance of Electrical Machines with Ferrite Magnets. *J. Phys. D: Appl. Phys.* **2021**, *54* (5), 054001.
- (14) Lopez-Ortega, A.; Lottini, E.; Fernandez, C. d. J.; Sangregorio, C. Exploring the Magnetic Properties of Cobalt-Ferrite Nanoparticles for the Development of a Rare-Earth-Free Permanent Magnet. *Chem. Mater.* **2015**, *27* (11), 4048–4056.
- (15) Saura-Múzquiz, M.; Eikeland, A. Z.; Stingaciu, M.; Andersen, H. L.; Granados-Mirallas, C.; Avdeev, M.; Luzin, V.; Christensen, M. Elucidating the Relationship between Nanoparticle Morphology, Nuclear/Magnetic Texture and Magnetic Performance of Sintered SrFe₁₂O₁₉ Magnets. *Nanoscale* **2020**, *12* (17), 9481–9494.
- (16) Maltoni, P.; Sarkar, T.; Varvaro, G.; Barucca, G.; Ivanov, S.; Peddis, D.; Mathieu, R. Towards Bi-Magnetic Nanocomposites as Permanent Magnets through the Optimization of the Synthesis and Magnetic Properties of SrFe₁₂O₁₉ Nanocrystallites. *J. Phys. D: Appl. Phys.* **2021**, *54* (12), 124004.
- (17) Mohseni, F.; Pullar, R. C.; Vieira, J. M.; Amaral, J. S. Bonded Ferrite-Based Exchange-Coupled Nanocomposite Magnet Produced by Warm Compaction. *J. Phys. D: Appl. Phys.* **2020**, *53* (49), 494003.
- (18) Kotnana, G.; Sayed, F.; Joshi, D. C.; Barucca, G.; Peddis, D.; Mathieu, R.; Sarkar, T. Novel Mixed Precursor Approach to Prepare Multiferroic Nanocomposites with Enhanced Interfacial Coupling. *J. Magn. Magn. Mater.* **2020**, *511*, 166792.
- (19) Granados-Mirallas, C.; Quesada, A.; Saura-Múzquiz, M.; Andersen, H. L.; Fernández, J. F.; Christensen, M. Expanding the Tunability and Applicability of Exchange-Coupled/Decoupled Magnetic Nanocomposites. *Mater. Chem. Front.* **2020**, *4* (4), 1222–1230.
- (20) Muscas, G.; Anil Kumar, P.; Barucca, G.; Concas, G.; Varvaro, G.; Mathieu, R.; Peddis, D. Designing New Ferrite/Manganite Nanocomposites. *Nanoscale* **2016**, *8* (4), 2081–2089.
- (21) Sayed, F.; Muscas, G.; Jovanovic, S.; Barucca, G.; Locardi, F.; Varvaro, G.; Peddis, D.; Mathieu, R.; Sarkar, T. Controlling Magnetic Coupling in Bi-Magnetic Nanocomposites. *Nanoscale* **2019**, *11* (30), 14256–14265.
- (22) Sayed, F.; Kotnana, G.; Muscas, G.; Locardi, F.; Comite, A.; Varvaro, G.; Peddis, D.; Barucca, G.; Mathieu, R.; Sarkar, T. Symbiotic, Low-Temperature, and Scalable Synthesis of Bi-Magnetic Complex Oxide Nanocomposites. *Nanoscale Adv.* **2020**, *2* (2), 851–859.
- (23) Coey, J. M. D. *Magnetism and Magnetic Materials*; Cambridge University Press: 2001.
- (24) Zeng, H.; Li, J.; Liu, J. P.; Wang, Z. L.; Sun, S. Exchange-Coupled Nanocomposite Magnets by Nanoparticle Self-Assembly. *Nature* **2002**, *420* (6914), 395–398.
- (25) Esir, S.; Junejo, Y.; Baykal, A.; Toprak, M.; Sözeri, H. SrFe₁₂O₁₉/Zn_{0.65}Ni_{0.25}Cu_{0.1}Fe₂O₄ Core-Shell Nanocomposite: Synthesis, Characterization and Catalytic Activity in Aqueous Solution. *J. Inorg. Organomet. Polym. Mater.* **2014**, *24* (4), 722–728.
- (26) Sarkar, T.; Muscas, G.; Barucca, G.; Locardi, F.; Varvaro, G.; Peddis, D.; Mathieu, R. Tunable Single-Phase Magnetic Behavior in Chemically Synthesized AFeO₃–MFe₂O₄ (A = Bi or La, M = Co or Ni) Nanocomposites. *Nanoscale* **2018**, *10* (48), 22990–23000.
- (27) Liu, W.; Zhang, Z.-d.; Liu, J.-p.; Chen, L.-j.; He, L.-l.; Liu, Y.; Sun, X.-k.; Sellmyer, D. J. Exchange Coupling and Remanence Enhancement in Nanocomposite Multilayer Magnets. *Adv. Mater.* **2002**, *14* (24), 1832–1834.
- (28) Sayed, F.; Kotnana, G.; Barucca, G.; Muscas, G.; Peddis, D.; Mathieu, R.; Sarkar, T. LaFeO₃–CoFe₂O₄ Bi-Magnetic Composite Thin Films Prepared Using an All-in-One Synthesis Technique. *J. Magn. Magn. Mater.* **2020**, *503*, 166622.
- (29) Jenuš, P.; Topole, M.; McGuiness, P.; Granados-Mirallas, C.; Stingaciu, M.; Christensen, M.; Kobe, S.; Žužek Rožman, K. Ferrite-Based Exchange-Coupled Hard-Soft Magnets Fabricated by Spark Plasma Sintering. *J. Am. Ceram. Soc.* **2016**, *99* (6), 1927–1934.
- (30) Pullar, R. C. Hexagonal Ferrites: A Review of the Synthesis, Properties and Applications of Hexaferrite Ceramics. *Prog. Mater. Sci.* **2012**, *57* (7), 1191–1334.
- (31) Coey, J. M. D. Hard Magnetic Materials: A Perspective. *IEEE Trans. Magn.* **2011**, *47* (12), 4671–4681.
- (32) Rodríguez-Carvajal, J. Recent Advances in Magnetic Structure Determination by Neutron Powder Diffraction. *Phys. B* **1993**, *192* (1–2), 55–69.
- (33) Normile, P. S.; Andersson, M. S.; Mathieu, R.; Lee, S. S.; Singh, G.; De Toro, J. A. Demagnetization Effects in Dense Nanoparticle Assemblies. *Appl. Phys. Lett.* **2016**, *109* (15), 152404.
- (34) Das, A.; Roychowdhury, A.; Pati, S. P.; Bandyopadhyay, S.; Das, D. Structural, Magnetic and Hyperfine Properties of Single-Phase SrFe₁₂O₁₉ Nanoparticles Prepared by a Sol–Gel Route. *Phys. Scr.* **2015**, *90* (2), 025802.
- (35) Anedda, R.; Cannas, C.; Musinu, A.; Pinna, G.; Piccaluga, G.; Casu, M. A Two-Stage Citric Acid–Sol/Gel Synthesis of ZnO/SiO₂ Nanocomposites: Study of Precursors and Final Products. *J. Nanopart. Res.* **2008**, *10* (1), 107–120.
- (36) Mamelì, V.; Musinu, A.; Ardu, A.; Ennas, G.; Peddis, D.; Niznansky, D.; Sangregorio, C.; Innocenti, C.; Thanh, N. T. K.; Cannas, C. Studying the Effect of Zn-Substitution on the Magnetic and Hyperthermic Properties of Cobalt Ferrite Nanoparticles. *Nanoscale* **2016**, *8* (19), 10124–10137.
- (37) Cannas, C.; Musinu, A.; Peddis, D.; Piccaluga, G. Synthesis and Characterization of CoFe₂O₄ Nanoparticles Dispersed in a Silica Matrix by a Sol–Gel Autocombustion Method. *Chem. Mater.* **2006**, *18* (16), 3835–3842.

- (38) Harikrishnan, V.; Ezhil Vizhi, R. A Study on the Extent of Exchange Coupling between $(\text{Ba}_{0.5}\text{Sr}_{0.5}\text{Fe}_{12}\text{O}_{19})_{1-x}(\text{CoFe}_2\text{O}_4)_x$ Magnetic Nanocomposites Synthesized by Solgel Combustion Method. *J. Magn. Magn. Mater.* **2016**, *418*, 217–223.
- (39) Obradors, X.; Solans, X.; Collomb, A.; Samaras, D.; Rodriguez, J.; Pernet, M.; Font-Altaba, M. Crystal Structure of Strontium Hexaferrite $\text{SrFe}_{12}\text{O}_{19}$. *J. Solid State Chem.* **1988**, *72* (2), 218–224.
- (40) Eikeland, A. Z.; Stingaciu, M.; Mamakhel, A. H.; Saura-Múzquiz, M.; Christensen, M. Enhancement of Magnetic Properties through Morphology Control of $\text{SrFe}_{12}\text{O}_{19}$ Nanocrystallites. *Sci. Rep.* **2018**, *8* (1), 7325.
- (41) Momma, K.; Izumi, F. VESTA: A Three-Dimensional Visualization System for Electronic and Structural Analysis. *J. Appl. Crystallogr.* **2008**, *41* (3), 653–658.
- (42) López-Ortega, A.; Estrader, M.; Salazar-Alvarez, G.; Roca, A. G.; Nogués, J. Applications of Exchange Coupled Bi-Magnetic Hard/Soft and Soft/Hard Magnetic Core/Shell Nanoparticles. *Phys. Rep.* **2015**, *553*, 1–32.
- (43) O'Grady, K.; Chantrell, R. W. Remanence Curves of Fine Particles Systems I: Experimental Studies, 1992.
- (44) Walker, M.; Majo, P. I.; O'Grady, K.; Charles, S. W.; Chantrell, R. W. The Magnetic Properties of Single-Domain Particles with Cubic Anisotropy. II. Remanence Curves. *J. Phys.: Condens. Matter* **1993**, *5* (17), 2793.
- (45) Peddis, D.; Jönsson, P. E.; Laureti, S.; Varvaro, G. *Magnetic Interactions* **2014**, 129–188.
- (46) Quesada, A.; Granados-Miralles, C.; López-Ortega, A.; Erokhin, S.; Lottini, E.; Pedrosa, J.; Bollero, A.; Aragón, A. M.; Rubio-Marcos, F.; Stingaciu, M.; et al. M. Energy Product Enhancement in Imperfectly Exchange-Coupled Nanocomposite Magnets. *Adv. Electron. Mater.* **2016**, *2* (4), 1500365.
- (47) Granados-Miralles, C.; Saura-Múzquiz, M.; Andersen, H. L.; Quesada, A.; Ahlburg, J. V.; Dippel, A.-C.; Canévet, E.; Christensen, M. Approaching Ferrite-Based Exchange-Coupled Nanocomposites as Permanent Magnets. *ACS Appl. Nano Mater.* **2018**, *1* (7), 3693–3704.
- (48) Zhang, L.; Li, Z. Synthesis and Characterization of $\text{SrFe}_{12}\text{O}_{19}/\text{CoFe}_2\text{O}_4$ Nanocomposites with Core-Shell Structure. *J. Alloys Compd.* **2009**, *469* (1–2), 422–426.
- (49) Xia, A.; Ren, S.; Lin, J.; Ma, Y.; Xu, C.; Li, J.; Jin, C.; Liu, X. Magnetic Properties of Sintered $\text{SrFe}_{12}\text{O}_{19}$ – CoFe_2O_4 Nanocomposites with Exchange Coupling. *J. Alloys Compd.* **2015**, *653*, 108–116.
- (50) Fullerton, E. E.; Jiang, J. S.; Bader, S. D. Hard/Soft Magnetic Heterostructures: Model Exchange-Spring Magnets. *J. Magn. Magn. Mater.* **1999**, *200* (1–3), 392–404.
- (51) Fischbacher, J.; Kovacs, A.; Gusenbauer, M.; Oezelt, H.; Exl, L.; Bance, S.; Schrefl, T. Micromagnetics of Rare-Earth Efficient Permanent Magnets. *J. Phys. D: Appl. Phys.* **2018**, *51* (19), 193002.
- (52) Omelyanchik, A.; Levada, K.; Pshenichnikov, S.; Abdolrahim, M.; Baricic, M.; Kapitonova, A.; Galieva, A.; Sukhikh, S.; Astakhova, L.; Antipov, S.; et al. Green Synthesis of Co-Zn Spinel Ferrite Nanoparticles: Magnetic and Intrinsic Antimicrobial Properties. *Materials* **2020**, *13* (21), 5014.
- (53) Albino, M.; Fantechi, E.; Innocenti, C.; López-Ortega, A.; Bonanni, V.; Campo, G.; Pineider, F.; Gurioli, M.; Arosio, P.; Orlando, T.; et al. Role of Zn^{2+} Substitution on the Magnetic, Hyperthermic, and Relaxometric Properties of Cobalt Ferrite Nanoparticles. *J. Phys. Chem. C* **2019**, *123* (10), 6148–6157.